A Letters Journal Exploring
the Frontiers of Physics

September 2016

EPL, **115** (2016) 65001
doi: 10.1209/0295-5075/115/65001

www.epljournal.org

Observation of interspecies ion separation in inertial-confinement-fusion implosions

S. C. Hsu[1], T. R. Joshi[1], P. Hakel[1], E. L. Vold[1], M. J. Schmitt[1], N. M. Hoffman[1], R. M. Rauenzahn[1], G. Kagan[1], X.-Z. Tang[1], R. C. Mancini[2], Y. Kim[1] and H. W. Herrmann[1]

[1] *Los Alamos National Laboratory - Los Alamos, NM 87545, USA*
[2] *Physics Department, University of Nevada - Reno, NV 89557, USA*

received 9 August 2016; accepted in final form 5 October 2016
published online 24 October 2016

PACS 52.57.-z – Laser inertial confinement
PACS 52.25.Fi – Transport properties
PACS 52.65.-y – Plasma simulation

Abstract – We report direct experimental evidence of interspecies ion separation in direct-drive, inertial-confinement-fusion experiments on the OMEGA laser facility. These experiments, which used plastic capsules with D_2/Ar gas fill (1% Ar by atom), were designed specifically to reveal interspecies ion separation by exploiting the predicted, strong ion thermo-diffusion between ion species of large mass and charge difference. Via detailed analyses of imaging x-ray-spectroscopy data, we extract Ar-atom-fraction radial profiles at different times, and observe both enhancement and depletion compared to the initial 1%-Ar gas fill. The experimental results are interpreted with radiation-hydrodynamic simulations that include recently implemented, first-principles models of interspecies ion diffusion. The experimentally inferred Ar-atom-fraction profiles agree reasonably, but not exactly, with calculated profiles associated with the incoming and rebounding first shock.

Interspecies ion separation has been proposed as a potential fusion-yield degradation mechanism in inertial-confinement-fusion (ICF) implosions [1–3]. Several ICF experimental campaigns [4–11] have reported yield or yield-ratio anomalies where interspecies ion separation within the hot spot is a possible explanation. Meanwhile, first-principles analytic theories for multi-ion-species diffusion [1,2,12–16] have been developed, some of which have been implemented into ICF implosion codes [17,18], enabling us to quantitatively assess the magnitude of interspecies ion separation and yield degradation in ICF implosions. In addition, ion-Fokker-Planck [19,20] and particle-in-cell kinetic simulations [3,21,22] are being used to address this problem, and are particularly appropriate for more-kinetic scenarios, *e.g.*, exploding pushers, hot-spot formation in ignition capsules, hohlraum plasmas, or near steep gradients at shock fronts and material interfaces. We do not address the question here of whether interspecies ion separation substantially affects the yield in ignition-class implosions on the National Ignition Facility [23], but point out that this and related work will help establish a validated capability to answer the question in a quantitative manner.

The purpose of this work is to complement and expand upon prior ICF experimental campaigns that relied on yield or yield-ratio anomalies as evidence for species separation. Here, based on direct-drive ICF implosions on the OMEGA laser facility [24], we provide direct, spatially resolved experimental evidence of interspecies ion separation via detailed analyses of imaging x-ray-spectroscopy data, which are less sensitive to other potential causes of yield degradation in an ICF implosion. In this work: 1) we exploit recently developed analytic theory [14,15] of interspecies ion diffusion to design an ICF implosion that maximizes interspecies ion diffusion, such that it is observable via x-ray diagnostics; 2) rather than focusing on separation between fuel species, *e.g.*, D/^{3}He or D/T, we use D and a trace amount of Ar, where both the choice of Ar itself and its pre-fill concentration are chosen to maximize the expected interspecies diffusion coefficient; and 3) we aim for a more-collisional implosion so that interpretations using the recently formulated interspecies-ion-diffusion theories are appropriate. The main results in this letter are the first direct identification of interspecies ion separation in an ICF implosion based on the analyses of spatially resolved x-ray-spectroscopy data, observation

Table 1: Summary of shots analyzed for this letter. Yield (DD-n) and burn-weighted ion temperature $\langle T_i \rangle$ are from the 12 m neutron time-of-flight scintillator, and neutron bang times (BT) and burn widths (BW) are from the cryogenic neutron temporal diagnostic (cryoNTD). Note that BT corresponds to compression burn in these implosions.

Shot #	Laser energy (kJ)	Capsule OD (μm)/ CH thickness (μm)	D_2/Ar fill (atm)	Ar (atom%)	Yield (DD-n)	$\langle T_i \rangle$ (keV)	BT (ns)	BW (ps)
78197	21.2	863.2/13.1	5.0	1.01	1.18E11	6.43	1.317	110
78199	21.1	861.8/13.1	5.0	1.01	1.35E11	6.48	1.313	116
78201	26.2	874.5/14.8	3.18	1.12	8.06E10	6.93	1.355	120

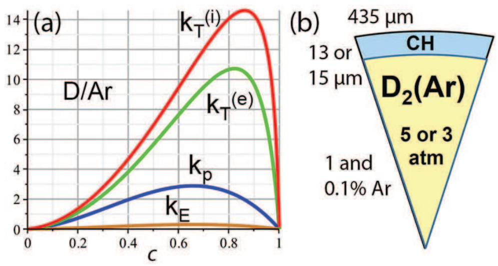

Fig. 1: (Colour online) (a) D/Ar interspecies diffusion ratios *vs.* $c \equiv \rho_D/(\rho_D + \rho_{Ar})$ for ion thermo-diffusion $k_T^{(i)}$, electron thermo-diffusion $k_T^{(e)}$, baro-diffusion k_p, and electro-diffusion k_E, assuming charge state $Z_{Ar} = 18$. (b) We shot four target types: 15 μm/3 atm and 13 μm/5 atm, with 1% or 0.1% Ar by atom.

of spatially non-uniform Ar-concentration enhancement and depletion (compared to the spatially uniform pre-fill of 1% Ar by atom) during the implosion, and reasonable agreement of the experimentally inferred Ar-atom-fraction profiles with radiation-hydrodynamic simulations that model interspecies ion diffusion from first principles.

We briefly discuss the theory that guided these experiments. The diffusive mass flux of the lighter ions relative to the center of mass in a plasma with two ion species can be written as [14,15] $\vec{i} = -\rho D[\nabla c + k_p \nabla \log p_i + (ek_E/T_i)\nabla\Phi + k_T^{(i)}\nabla \log T_i + k_T^{(e)}\nabla \log T_e]$, where ρ is the total mass density, D the classical diffusion coefficient, $c \equiv \rho_l/\rho$ the lighter-ion mass concentration, p_i the ion pressure, T_i and T_e the ion and electron temperatures, respectively, Φ the electric potential, and k_p, k_E, $k_T^{(i)}$, $k_T^{(e)}$ the diffusion ratios for baro-diffusion, electro-diffusion, ion thermo-diffusion, and electron thermo-diffusion, respectively; $\vec{i}$ can also be written in terms of molar-concentration gradients [16]. Because the theory predicts larger diffusion ratios for ion species with a large mass and charge difference [15], we focused on a D/Ar mixture (rather than D/^{3}He or D/T). We chose Ar in particular because of its proven usefulness as an x-ray spectroscopic tracer in ICF implosions [25–31]. We evaluated the diffusion ratios [15] for a D/Ar mixture *vs.* c (fig. 1(a)); $k_T^{(i)}$ is the largest ratio and maximizes at $c = \rho_D/(\rho_D + \rho_{Ar}) \approx 0.84$, corresponding to Ar number fraction $f_{Ar} \equiv n_{Ar}/(n_{Ar} + n_D) \approx (1-c)/(1+19c) \approx 1\%$.

Thus, we focused our attention on an implosion design with large ∇T_i and $f_{Ar} \approx 1\%$ to maximize ion thermo-diffusion. Furthermore, we wanted relatively high T_i and D while keeping the Ar-D mean free path much smaller than the hot-spot size for most of the implosion. Although the theory [14–16] is not strictly correct within a shock front, it should nevertheless capture the qualitative, leading-order effects on interspecies ion separation during the passage and rebound of the first incoming shock.

We performed 1D HYDRA [32] simulations of direct-drive OMEGA implosions with a 1 ns square pulse to arrive at the capsule designs in fig. 1(b). Table 1 summarizes the as-shot laser and target parameters and neutron-based measurements. To evaluate the amount of expected species separation, we also performed pre-shot 1D simulations using xRAGE [17] with its recently implemented two-ion-species transport model [16]. All our pre-shot xRAGE results showed relative deviations in f_{Ar} of $\geq 20\%$, in some cases much larger, from the initial values ($f_{Ar} = 0.01$ or 0.001) over much of the implosion, giving us confidence that we could resolve the species separation based on error bars achieved in previous analyses of imaging x-ray-spectroscopy data.

The primary diagnostics are two x-ray multi-monochromatic imagers (MMI) [33] with quasi-orthogonal views (mounted on TIMs 3 and 4, where TIM stands for a "ten-inch manipulator" diagnostic port), a streaked x-ray spectrometer (TIM 1), and a time- and space-integrated, absolutely calibrated x-ray spectrometer (TIM 2). Standard neutron diagnostics and full-aperture backscatter systems were also fielded. The MMIs used 10 μm diameter pinholes, setting the spatial resolution at $\gtrsim 10\,\mu$m, and recorded data on x-ray framing cameras between 3.3 and 5.5 keV around the time of first-shock convergence. Each camera recorded four frames per shot at different times; frame trigger times are given in the figure captions. We obtained analyzable MMI data for several shots with initial $f_{Ar} \approx 1\%$ (table 1), and used the Ar-Heβ (3.68 keV), Lyβ (3.94 keV), and Lyγ (4.15 keV) lines in our spectroscopic analyses. Shots with initial $f_{Ar} \approx 0.1\%$, predicted to have much reduced ion thermo-diffusion, provided weaker spectral lines.

The key objective and result of this work is the experimental inference of f_{Ar} *vs.* radius r. Deviation from the spatially uniform target-pre-fill value constitutes proof of

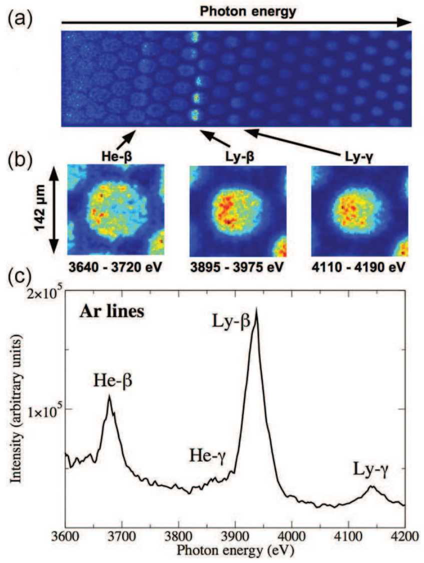

Fig. 2: (Colour online) (a) MMI data showing an array of spectrally resolved implosion-core pinhole images (intensity, arbitrary units) *vs.* photon energy along the x-axis for shot 78199, TIM 3, frame 2 (1.14 ns trigger time), (b) Ar Heβ, Lyβ, and Lyγ narrow-band images constructed from 80 eV wide (as given below each image) vertical strips of the data in (a). (c) Space-integrated spectrum from (a) before continuum subtraction.

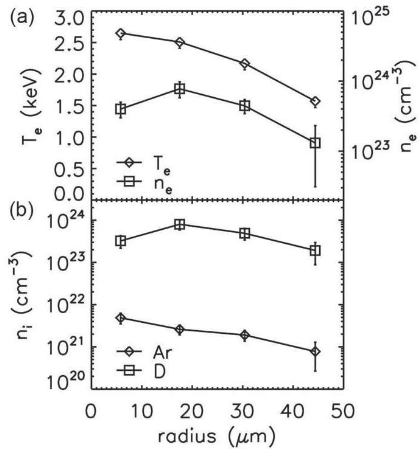

Fig. 3: (a) Electron temperature and density and (b) D and Ar ion densities *vs.* radius, from analysis of MMI data (shot 78199, TIM 3, frame 2, 1.14 ns trigger time). See text for explanation of error bars.

interspecies ion separation. Figures 2 and 3 illustrate the key steps of the MMI data processing and analyses required to arrive at $f_{Ar}(r)$. MMI data processing to obtain narrow-band images (fig. 2(b)) is based on the method of refs. [29,31], and [34]. Extraction of electron density n_e and temperature T_e *vs.* r are based on the emissivity-analysis method of ref. [28]. Figure 2(a) shows one frame of MMI data after it has been converted from film density to intensity (arbitrary units). The photon-energy dependence of the MMI data is corrected using streaked and absolutely calibrated spectral data[1]. Figure 2(b) shows the narrow-band images constructed from the data in fig. 2(a), and fig. 2(c) shows the space-integrated spectrum from fig. 2(a) before continuum subtraction.

The next step is to extract n_e and T_e radial profiles. Abel inversion is applied to each narrow-band image, *e.g.*, fig. 2(b), giving argon emissivity (with continuum subtracted) *vs.* r for four radial zones of approximately 10 μm width (set by both the size of MMI pinholes and spectral signal-to-noise considerations for each zone), at the time of the particular MMI frame. The time is approximately known based on the experimental trigger time of each frame of the x-ray framing camera, but due to cable delays and the finite time of the sweep across the camera's photocathode strips, we regard the quoted times as having an uncertainty ~ 50 ps. The Ar-Heβ and Lyβ emissivity profiles are analyzed to provide n_e and T_e *vs.* r (fig. 3(a)) based on comparisons with detailed atomic-physics models. The underlying atomic database was generated via the fully relativistic path in the Los Alamos suite of codes RATS, ACE, and GIPPER [35,36], followed by the collisional-radiative code ATOMIC [36–38]. The resulting NLTE (non-local thermal equilibrium) spectral data were used in the intensity and emissivity analyses of the MMI data (figs. 3, 4(a), (b)), as well as in the forward modeling of space-resolved spectra and narrow-band images by the FESTR spectral post-processing code [39,40]. Error bars for T_e are obtained based on the greater of the T_e resolution (100 eV) in the atomic database mentioned above or the standard deviation of T_e (*e.g.*, average of 63 eV for the four radial zones for shot 78199, TIM 3, frame 2) as determined from the theoretical emissivity ratio of Lyβ/Heβ at four different values of n_e (5×10^{23}, 8×10^{23}, 1×10^{24}, and 2×10^{24} cm^{-3}) in our regime of interest. Error bars for n_e are obtained based on the greater of the uncertainties in the T_e (100 eV) and n_e resolutions (1–2×10^{23} cm^{-3}, depending on the density) in the database, or the standard deviation in n_e (*e.g.*, average of 1.1×10^{23} cm^{-3} for the four radial zones for shot 78199, TIM 3, frame 2) from assuming slightly higher and lower values of n_e in the central zone (*e.g.*, $4 \pm 1 \times 10^{23}$ cm^{-3} for shot 78199, TIM 3, frame 2), which is derived from the line broadening of each of the three Ar lines from the space-integrated spectrum.

The argon density n_{Ar} is determined using $n_{Ar} = n_u/F_u(T_e, n_e)$, where n_u and F_u are the upper-level number densities and fractional populations, respectively, of the particular line transition being used [41]. $F_u(T_e, n_e)$ is retrieved from the atomic database based on the previously determined $n_e(r)$ and $T_e(r)$. Since the spectral lines are sufficiently optically thin [28], n_u (arbitrary

[1]The MMI data is corrected as follows. First, the streaked x-ray-spectroscopy data (SSCA) is corrected by matching the time-integrated SSCA data to the space- and time-integrated, absolutely calibrated x-ray-spectroscopy data (XRS2). Then the space-integrated MMI spectrum is corrected to match the corrected SSCA data at the time of the MMI data.

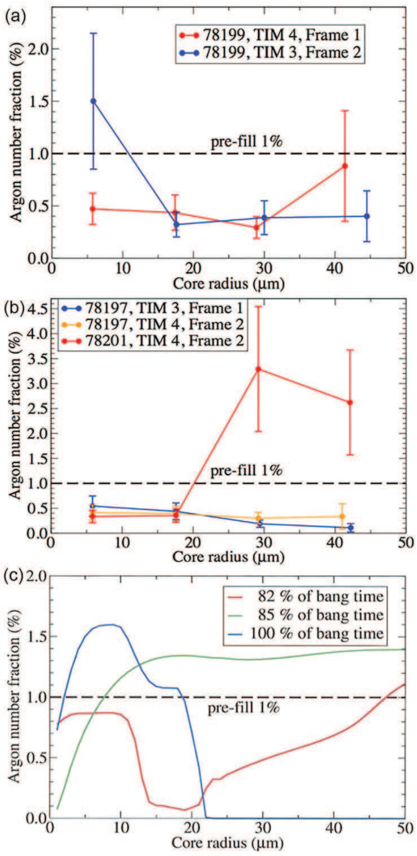

Fig. 4: (Colour online) Argon number fraction f_{Ar} *vs.* r for (a) shot 78199 (red $\approx 1.10\,\text{ns} = 84\%$ of BT, blue $\approx 1.14\,\text{ns} = 87\%$ of BT), (b) shots 78197 and 78201 (blue $\approx 1.08\,\text{ns} = 82\%$ of BT, orange $\approx 1.09\,\text{ns} = 83\%$ of BT, red $\approx 1.18\,\text{ns} = 87\%$ of BT), and (c) 1D post-shot xRAGE simulation (shot 78199) including a two-ion-species transport model [16].

units) is extracted based on its proportionality to the corresponding observed line intensities, which are obtained from the space-resolved spectra extracted from annular regions of the implosion-core image by numerically integrating the area under the line after continuum subtraction. Finally, the known pre-fill amount of Ar closes the system of linear equations relating $n_u(r)$ to $n_{Ar}(r)$ [41]. Error bars for n_{Ar} are from propagation of uncertainties in n_u (*e.g.*, 9%, 6%, 7%, and 8% from the innermost to outermost radial zone for shot 78199, TIM 3, frame 2) and $F_u(T_e, n_e)$ (*e.g.*, 25%, 22%, 20%, and 54% from the innermost to outermost radial zone for shot 78199, TIM 3, frame 2). The deuterium density n_D is inferred from quasi-neutrality $n_e = Z_D n_D + Z_{Ar} n_{Ar}$, and finally $f_{Ar} \equiv n_{Ar}/(n_{Ar} + n_D)$. Error bars for n_D and f_{Ar} use the propagated errors from n_e and n_{Ar}, and n_{Ar} and n_D, respectively. Figure 3 shows an example of n_e, T_e, n_{Ar}, and n_D *vs.* r, and figs. 4(a) and (b) show $f_{Ar}(r)$ from different shots and MMI views and times. Results shown are the averages from the Ar-Heβ, Lyβ, and Lyγ lines. The non-uniform spatial profiles of f_{Ar} and their deviation from the initial pre-fill value from several different shots and times constitute proof of interspecies ion separation between the D and Ar, which is the main result of this letter.

To build confidence in our conclusions, we apply the same analysis procedure to synthetic Ar-Heβ, Lyβ, and Lyγ images and space-resolved spectra. The synthetic data are generated using the FESTR code [40], using the data in fig. 3 and assuming 1D spherical symmetry, for two cases: i) n_{Ar} as shown in fig. 3(b) and ii) spatially uniform $f_{Ar} = 0.01$ with equal $n_D + n_{Ar}$ as in i). In both cases, we extract $f_{Ar}(r)$ in good agreement with the $f_{Ar}(r)$ in the synthetic data. This demonstrates that our analysis accurately extracts $f_{Ar}(r)$ and is also able to distinguish between species separation *vs.* no species separation.

We also note some limitations of our analysis. Firstly, our analysis assumes 1D spherical symmetry, introducing possible errors if the implosion has significant 2D and/or 3D structure. While our implosions appear fairly round, and quasi-orthogonal MMI views at similar times yield similar results (*e.g.*, shot 78197, blue and orange curves in fig. 4(b)), small-scale non-uniformities are clearly visible (*e.g.*, fig. 2(b)). We assessed the effect of non-uniformities for shot 78199 (TIM 3, frame 2) by dividing the narrow-band images of fig. 2(b) into three wedges of 120° each and doing independent analysis on each wedge to obtain n_e and T_e profiles; the standard deviations of $n_e(r)$ and $T_e(r)$ across the three wedges are similar to the error bars already considered (as shown in fig. 3) and thus would not substantially increase the final error bars shown in fig. 4. Future work should employ both 2D [31] and 3D [42] reconstruction techniques to further assess both 2D and 3D effects on our analysis. Secondly, unaccounted-for CH shell mix into the hot spot affects the species balance in the quasi-neutrality condition used in our analysis by causing overestimates of the inferred n_D, which affects the inferred f_{Ar}. However, we have estimated that the local CH fraction in the hot spot must exceed an unrealistically large value $\sim 10\%$ before it could affect our conclusion of D/Ar separation presented in figs. 4(a) and (b). Finally, our use of the known initial amount of Ar in the fuel region to infer absolute n_{Ar} from n_u (arbitrary units) means that n_{Ar} is overestimated if Ar leaks into the shell. The latter could be a possible explanation for why $f_{Ar}(r) < 1\%$ everywhere for shot 78197 (fig. 4(b)), keeping in mind that $f_{Ar}(r)$ is extracted only from regions with visible, analyzable Ar spectral emission. Resolution of the shell/gas-mix issues requires further work, including the use of N-species ion-diffusion models that can model both the D/Ar separation and gas/shell mix.

Next, we interpret our results via a post-shot, 1D simulation of shot 78199 using xRAGE [17] with a two-ion-species transport model [16]. Figure 4(c) shows $f_{Ar}(r)$ for shot 78199, revealing that f_{Ar} is reduced ahead of the incoming first shock and enhanced behind it (green and red curves of fig. 4(c)). After shock reflection (at $\approx 1.18\,\text{ns}$ and $\approx 87\%$ of neutron bang time in the simulation), f_{Ar} is enhanced throughout much of the hot spot (up to $\approx 20\,\mu\text{m}$) through neutron bang time (blue curve of fig. 4(c)). Furthermore, when ion thermo-diffusion, which is the strongest expected contributor to interspecies separation between D and Ar, is turned off in the calculation, the f_{Ar} enhancement and depletion largely disappear. Independently, these effects are also seen in post-shot simulations from another radiation-hydrodynamics code, to which a multi-ion-species diffusion model has been added [43] and recently updated to include ion thermo-diffusion [15,44–46]. Additional detailed comparisons between our data and simulation results from both codes will be reported elsewhere. While detailed validation is beyond the scope of this work, note that there is reasonable agreement between the data and two key aspects of the post-shot simulation of shot 78199: 1) the peak magnitude of f_{Ar} ($\approx$ 1.5%), *i.e.*, compare maxima of blue curves in figs. 4(a) and (c), and 2) the qualitative evolution of f_{Ar}, in that f_{Ar} is below 1% nearer the origin at an earlier time (red curves of figs. 4(a) and (c)) and above 1% nearer the origin at a later time (blue curves of figs. 4(a) and (c)). Differences in the details of the f_{Ar}-profile evolution between the observations and xRAGE simulation could arise because 1) there could be more D enhancement ahead of the shock front than the xRAGE prediction due to kinetic effects near the shock front, and 2) shell mix, which affects f_{Ar} through an altered species balance in the quasi-neutrality condition, is not included in the xRAGE simulation.

Additional evidence supports our identification of interspecies ion separation. The FESTR code [40] is used to find the best spectral fit to radially resolved Ar spectral data. In all cases examined, when f_{Ar} is allowed to be a free parameter in the fitting instead of being fixed at the initial pre-fill value of 1%, the fit is improved, *e.g.*, 36% improvement in normalized χ^2 for the third radial zone (corresponding to $r \approx 30\,\mu$m) of the data in fig. 2.

In conclusion, we have reported direct experimental evidence for interspecies ion separation in an ICF implosion, via detailed analyses of imaging x-ray-spectroscopy data. These direct-drive OMEGA implosions of plastic capsules with D_2/Ar gas fill were designed to maximize interspecies ion thermo-diffusion between ion species of large mass and charge difference. This campaign benefitted from pre- and post-shot radiation-hydrodynamic simulations including a first-principles treatment of interspecies ion diffusion. The simulations show that f_{Ar} is depleted and enhanced, respectively, in front of and behind the first incoming shock, with f_{Ar} enhancement persisting at the center from first-shock convergence through neutron bang time. Our data agree reasonably well with the calculated effects on $f_{Ar}(r)$ due to the incoming and rebounding first shock, but more detailed validation, which is beyond the scope of this work, is needed. The experimental Ar K-shell spectral signatures are overtaken by bremsstrahlung continuum by the time of neutron bang time (around the time of peak compression), and thus we are unable to report whether interspecies separation is observed through bang time. Nevertheless, this first result using x-ray spectroscopy to detect interspecies ion separation encourages further work toward establishing a validated capability to address its role in yield degradation of ignition-scale ICF implosions.

* * *

We acknowledge R. Aragonez, T. Archuleta, J. Cobble, J. Fooks, V. Glebov, M. Schoff, T. Sedillo, C. Sorce, R. Staerker, N. Whiting, B. Yaakobi, and the OMEGA operations team for their support in experimental planning, execution, and providing processed x-ray and neutron data. This work was supported by the LANL ICF and ASC (Advanced Simulation and Computing) Programs under U.S. Department of Energy contract no. DE-AC52-06NA25396.

REFERENCES

[1] Amendt P., Landen O. L., Robey H. F., Li C. K. and Petrasso R. D., *Phys. Rev. Lett.*, **105** (2010) 115005.

[2] Amendt P., Wilks S. C., Bellei C., Li C. K. and Petrasso R. D., *Phys. Plasmas*, **18** (2011) 056308.

[3] Bellei C., Amendt P. A., Wilks S. C., Haines M. G., Casey D. T., Li C. K., Petrasso R. and Welch D. R., *Phys. Plasmas*, **20** (2013) 012701.

[4] Rygg J. R., Frenje J. A., Li C. K., Séguin F. H., Petrasso R. D., Delettrez J. A., Glebov V. Y., Goncharov V. N., Meyerhofer D. D., Regan S. P., Sangster T. C. and Stoeckl C., *Phys. Plasmas*, **13** (2006) 052702.

[5] Wilson D. C., Kyrala G. A., Benage J. F., Wysocki F. J., Gunderson M. A., Garbett W. J., Glebov V. Yu., Frenje J., Yaakobi B., Herrmann H. W., Cooley J. H., Welser-Sherrill L., Horsfield C. J. and Roberts S. A., *J. Phys.: Conf. Ser.*, **112** (2008) 022015.

[6] Dodd E. S., Benage J. F., Kyrala G. A., Wilson D. C., Wysocki F. J., Seka W., Glebov V. Y., Stoeckl C. and Frenje J. A., *Phys. Plasmas*, **19** (2012) 042703.

[7] Herrmann H. W., Langenbrunner J. R., Mack J. M., Cooley J. H., Wilson D. C., Evans S. C., Sedillo T. J., Kyrala G. A., Caldwell S. E., Young C. S., Nobile A., Wermer J., Paglieri S., McEvoy A. M., Kim Y., Batha S. H., Horsfield C. J., Drew D., Garbett W., Rubery M., Glebov V. Y., Roberts S. and Frenje J. A., *Phys. Plasmas*, **16** (2009) 056312.

[8] Casey D. T., Frenje J. A., Gatu Johnson M., Manuel M. J.-E., Rinderknecht H. G., Sinenian N., Séguin F. H., Li C. K., Petrasso R. D., Radha P. B., Delettrez J. A., Glebov V. Y., Meyerhofer D. D., Sangster T. C., McNabb D. P., Amendt P. A., Boyd R. N., Rygg J. R., Herrmann H. W., Kim Y. H. and Bacher A. D., *Phys. Rev. Lett.*, **108** (2012) 075002.

[9] Rinderknecht H. G., Sio H., Li C. K., Hoffman N., Zylstra A. B., Rosenberg M. J., Frenje J. A., Gatu Johnson M., Séguin F. H., Petrasso R. D., Betti R., Yu Glebov V., Meyerhofer D. D., Sangster T. C., Seka W., Stoeckl C., Kagan G., Molvig K., Bellei C., Amendt P., Landen O.,

Rygg J. R., Smalyuk V. A., Wilks S., Greenwood A. and Nikroo A., *Phys. Plasmas*, **21** (2014) 056311.

[10] Rosenberg M. J., Séguin F. H., Amendt P. A., Atzeni S., Rinderknecht H. G., Hoffman N. M., Zylstra A. B., Li C. K., Sio H., Gatu Johnson M., Frenje J. A., Petrasso R. D., Glebov V. Y., Stoeckl C., Seka W., Marshall F. J., Delettrez J. A., Sangster T. C., Betti R., Wilks S. C., Pino J., Kagan G., Molvig K. and Nikroo A., *Phys. Plasmas*, **22** (2015) 062702.

[11] Rinderknecht H. G., Rosenberg M. J., Li C. K., Hoffman N. M., Kagan G., Zylstra A. B., Sio H., Frenje J. A., Gatu Johnson M., Séguin F. H., Petrasso R. D., Amendt P., Bellei C., Wilks S., Delettrez J., Glebov V. Y., Stoeckl C., Sangster T. C., Meyerhofer D. D. and Nikroo A., *Phys. Rev. Lett.*, **114** (2015) 025001.

[12] Amendt P., Bellei C. and Wilks S., *Phys. Rev. Lett.*, **109** (2012) 075002.

[13] Kagan G. and Tang X. Z., *Phys. Rev. Lett.*, **109** (2012) 269501.

[14] Kagan G. and Tang X.-Z., *Phys. Plasmas*, **19** (2012) 082709.

[15] Kagan G. and Tang X.-Z., *Phys. Lett. A*, **378** (2014) 1531.

[16] Molvig K., Simakov A. N. and Vold E. L., *Phys. Plasmas*, **21** (2014) 092709.

[17] Gittings M., Weaver R., Clover M., Betlach T., Byrne N., Coker R., Dendy E., Hueckstaedt R., New K., Oakes W. R., Ranta D. and Stefan R., *Comput. Sci. Discov.*, **1** (2008) 015005.

[18] Vold E. L., Joglekar A. S., Ortega M. I., Moll R., Fenn D. and Molvig K., *Phys. Plasmas*, **22** (2015) 112708.

[19] Larroche O., *Phys. Plasmas*, **19** (2012) 122706.

[20] Inglebert A., Canaud B. and Larroche O., *EPL*, **107** (2014) 65003.

[21] Bellei C., Rinderknecht H., Zylstra A., Rosenberg M., Sio H., Li C. K., Petrasso R., Wilks S. C. and Amendt P. A., *Phys. Plasmas*, **21** (2014) 056310.

[22] Kwan T., Le A., Schmitt M., Herrmann H. and Batha S., *Bull. Am. Phys. Soc.*, **60** (2015) 324.

[23] Edwards M. J., Patel P. K., Lindl J. D., Atherton L. J., Glenzer S. H., Haan S. W., Kilkenny J. D., Landen O. L., Moses E. I., Nikroo A., Petrasso R., Sangster T. C., Springer P. T., Batha S., Benedetti R., Bernstein L., Betti R., Bleuel D. L., Boehly T. R., Bradley D. K., Caggiano J. A., Callahan D. A., Celliers P. M., Cerjan C. J., Chen K. C., Clark D. S., Collins G. W., Dewald E. L., Divol L., Dixit S., Doeppner T., Edgell D. H., Fair J. E., Farrell M., Fortner R. J., Frenje J., Gatu Johnson M. G., Giraldez E., Glebov V. Y., Grim G., Hammel B. A., Hamza A. V., Harding D. R., Hatchett S. P., Hein N., Herrmann H. W., Hicks D., Hinkel D. E., Hoppe M., Hsing W. W., Izumi N., Jacoby B., Jones O. S., Kalantar D., Kauffman R., Kline J. L., Knauer J. P., Koch J. A., Kozioziemski B. J., Kyrala G., LaFortune K. N., Pape S. L., Leeper R. J., Lerche R., Ma T., MacGowan B. J., MacKinnon A. J., Macphee A., Mapoles E. R., Marinak M. M., Mauldin M., McKenty P. W., Meezan M., Michel P. A., Milovich J., Moody J. D., Moran M., Munro D. H., Olson C. L., Opachich K., Pak A. E., Parham T., Park H.-S., Ralph J. E., Regan S. P., Remington B., Rinderknecht H., Robey H. F., Rosen M., Ross S., Salmonson J. D., Sater J., Schneider D. H., Sguin F. H., Sepke S. M., Shaughnessy D. A., Smalyuk V. A., Spears B. K., Stoeckl C., Stoeffl W., Suter L., Thomas C. A., Tommasini R., Town R. P., Weber S. V., Wegner P. J., Widman K., Wilke M., Wilson D. C., Yeamans C. B. and Zylstra A., *Phys. Plasmas*, **20** (2013) 070501.

[24] Boehly T. R., Brown D. L., Craxton R. S., Keck R. L., Knauer J. P., Kelly J. H., Kessler T. J., Kumpan S. A., Loucks S. J., Letzring S. A., Marshall F. J., McCrory R. L., Morse S. F. B., Seka W., Soures J. M. and Verdon C. P., *Opt. Commun.*, **133** (1997) 495.

[25] Haynes D. A., Garber D. T., Hooper C. F., Mancini R. C., Lee Y. T., Bradley D. K., Delettrez J., Epstein R. and Jaanimagi P. A., *Phys. Rev. E*, **53** (1996) 1042.

[26] Golovkin I., Mancini R., Louis S., Ochi Y., Fujita K., Nishimura H., Shirga H., Miyanaga N., Azechi H., Butzbach R., Uschmann I., Förster E., Delettrez J., Koch J., Lee R. W. and Klein L., *Phys. Rev. Lett.*, **88** (2002) 045002.

[27] Regan S. P., Delettrez J. A., Epstein R., Jaanimagi P. A., Yaakobi B., Smalyuk V. A., Marshall F. J., Meyerhofer D. D., Seka W., Haynes D. A., Golovkin I. E. and Hooper C. F., *Phys. Plasmas*, **9** (2002) 1357.

[28] Welser-Sherrill L., Mancini R. C., Koch J. A., Izumi N., Tommasini R., Haan S. W., Haynes D. A., Golovkin I. E., MacFarlane J. J., Delettrez J. A., Marshall F. J., Regan S. P., Smalyuk V. A. and Kyrala G., *Phys. Rev. E*, **76** (2007) 056403.

[29] Nagayama T., Mancini R. C., Florido R., Tommasini R., Koch J. A., Delettrez J. A., Regan S. P. and Smalyuk V. A., *J. Appl. Phys.*, **109** (2011) 093303.

[30] Florido R., Mancini R. C., Nagayama T., Tommasini R., Delettrez J. A., Regan S. P. and Yaakobi B., *Phys. Rev. E*, **83** (2011) 066408.

[31] Nagayama T., Mancini R. C., Florido R., Mayes D., Tommasini R., Koch J. A., Delettrez J. A., Regan S. P. and Smalyuk V. A., *Phys. Plasmas*, **21** (2014) 050702.

[32] Marinak M. M., Kerbel G. D., Gentile N. A., Jones O., Munro D., Pollaine S., Dittrich T. R. and Haan S. W., *Phys. Plasmas*, **8** (2001) 2275.

[33] Koch J. A., Barbee T. W., Izumi N., Tommasini R., Mancini R. C., Welser L. A. and Marshall F. J., *Rev. Sci. Instrum.*, **76** (2005) 073708.

[34] Nagayama T., Mancini R. C., Mayes D., Tommasini R. and Florido R., *Rev. Sci. Instrum.*, **86** (2015) 113505.

[35] Sampson D. H., Zhang H. L. and Fontes C. J., *Phys. Rep.*, **477** (2009) 111.

[36] Fontes C. J., Zhang H. L., Abdallah J. jr., Clark R. E. H., Kilcrease D. P., Colgan J.,

Cunningham R. T., Hakel P., Magee N. H. and Sherrill M. E., *J. Phys. B*, **48** (2015) 144014.

[37] Abdallah J. jr. and Clark R. E. H., *Rate Equations for Plasmas in Non Local Thermodynamic Equilibrium*, Los Alamos Technical Report LA-11926 (1990).

[38] Fontes C. J., Colgan J. and Abdallah J. jr., in *Modern Methods in Collisional-Radiative Modeling of Plasmas*, edited by Ralchenko Yu. (Springer, Switzerland) 2016, pp. 17–50.

[39] Hakel P., Kyrala G. A., Bradley P. A., Krasheninnikova N. S., Murphy T. J., Schmitt M. J., Tregillis I. L., Kanzleieter R. J., Batha S. H., Fontes C. J., Sherrill M. E., Kilcrease D. P. and Regan S. P., *Phys. Plasmas*, **21** (2014) 063306.

[40] Hakel P., *Comput. Phys. Commun.*, **207** (2016) 415.

[41] Joshi T. R., *Hydrodynamic stability and Ti-tracer distribution in low-adiabatic OMEGA direct-drive implosions*, PhD Thesis, University of Nevada, Reno, 2015, `http://search.proquest.com/docview/1732683657`.

[42] Nagayama T., Mancini R. C., Florido R., Mayes D., Tommasini R., Koch J. A., Delettrez J. A., Regan S. P. and Smalyuk V. A., *Phys. Plasmas*, **19** (2012) 082705.

[43] Hoffman N. M., Zimmerman G. B., Molvig K., Rinderknecht H. G., Rosenberg M. J., Albright B. J., Simakov A. N., Sio H., Zylstra A. B., Gatu Johnson M., Sguin F. H., Frenje J. A., Li C. K., Petrasso R. D., Higdon D. M., Srinivasan G., Glebov V. Y., Stoeckl C., Seka W. and Sangster T. C., *Phys. Plasmas*, **22** (2015) 052707.

[44] Schunk R. W., *Rev. Geophys.*, **15** (1977) 429.

[45] Zhdanov V. M., *Transport Processeses in Multicomponent Plasma* (Taylor & Francis, New York) 2002.

[46] Paquette C., Pelletier C., Fontaine G. and Michaud G., *Astrophys. J. Suppl. Ser.*, **61** (1986) 177.